b3galt6 knock-out zebrafish recapitulate β3GalT6-deficiency disorders in human and reveal a trisaccharide proteoglycan linkage region

Sarah Delbaere[a], Adelbert De Clercq[a], Shuji Mizumoto[b], Fredrik Noborn[c,d], Jan Willem Bek[a], Lien Alluyn[a], Charlotte Gistelinck[e], Delfien Syx[a], Phil L. Salmon[f], Paul J. Coucke[a], Göran Larson[c,d], Shuhei Yamada[b], Andy Willaert[a,1], Fransiska Malfait[a,1,2]

[a]Center for Medical Genetics Ghent, Department of Biomolecular Medicine, Ghent University and Ghent University Hospital, Ghent, Belgium.

[b]Department of Pathobiochemistry, Faculty of Pharmacy, Meijo University, 150 Yagotoyama, Tempaku-ku, Nagoya, Aichi 468-8503, Japan.

[c]Department of Laboratory Medicine, Sahlgrenska Academy at the University of Gothenburg, Gothenburg, Sweden.

[d]Laboratory of Clinical Chemistry, Sahlgrenska University Hospital, Gothenburg, Sweden.

[e]Department of Orthopaedics and Sports Medicine, University of Washington, Seattle, WA98195.

[f]Bruker microCT, Kontich, Belgium.

[1]AW and FM contributed equally to this work.

[2]Corresponding author:

Fransiska Malfait

Center for Medical Genetics, Ghent University Hospital, 0K5

Corneel Heymanslaan 10, B-9000 Ghent, Belgium

Tel: +32-9-332 36 03

E-mail: Fransiska.Malfait@UGent.be

Keywords

b3galt6, zebrafish, trisaccharide linkage region, proteoglycans, linkeropathies

Author Contributions

SD, AW and FM designed the study; SD, ADC, SM, FN, JWB, LA and CG performed research; SM, PLS, GL, SY contributed new reagents or analytic tools; SD, ADC, SM, FN, JWB, LA, CG, DS, PLS, PJC, GL, SY, AW and FM analyzed data; SD, AW and FM wrote the paper; all authors reviewed the paper.

Abstract

Proteoglycans are structurally and functionally diverse biomacromolecules found abundantly on cell membranes and in the extracellular matrix. They consist of a core protein linked to glycosaminoglycan chains via a tetrasaccharide linkage region. Here, we show that CRISPR/Cas9-mediated *b3galt6* knock-out zebrafish, lacking galactosyltransferase II, which adds the third sugar in the linkage region, largely recapitulate the phenotypic abnormalities seen in human β3GalT6-deficiency disorders. These comprise craniofacial dysmorphism, generalized skeletal dysplasia, skin involvement and indications for muscle hypotonia. Disturbed collagen fibril organization was the most consistent ultrastructural characteristic throughout affected tissues. Strikingly, despite a strong reduction in glycosaminoglycan content, we identified a small amount of proteoglycans containing a unique linkage region consisting of only three sugars. This implies that formation of glycosaminoglycans with an immature linkage region is possible in a pathogenic context. Our study therefore unveils a novel rescue mechanism for β3GalT6-deficiency, opening new avenues for therapeutic intervention.

Introduction

Proteoglycans (PGs) comprise a group of complex biomacromolecules, consisting of a core protein and one or multiple glycosaminoglycan (GAG) side chains, that are ubiquitously expressed in the extracellular matrix (ECM) and on cell surfaces and basement membranes in vertebrate and invertebrate species (1-4). Besides their structural role, PGs act as mediators between the ECM and intracellular signaling pathways and contribute to development and tissue homeostasis, influencing a variety of cellular processes including cell fate determination, cell proliferation, migration, adhesion, differentiation and survival (5).

The PG superfamily is, depending on the composition of the GAG chains, subdivided into heparan sulfate (HS) and chondroitin/dermatan sulfate (CS/DS) PGs. These GAG chains are linear polysaccharides, composed of a repeated disaccharide unit consisting of an uronic acid and amino sugar. HSPGs, such as perlecan, syndecan and glypican, consist of repeating glucuronic acid (GlcA)- *N*-acetyl-glucosamine (GlcNAc) disaccharides. CSPGs consist of repeating GlcA- *N*-acetyl-galactosamine (GalNAc) disaccharides. DS is a stereoisomer of CS, in which GlcA is epimerized to iduronic acid (IdoA). In mammalian tissues, CS and DS chains are often present as hybrid CS-DS chains on PGs (e.g. decorin, biglycan) (6). Tightly controlled modifications, such as epimerization and sulfation reactions, further increase the structural and functional diversity of the HS and CS/DS PGs (7, 8). GAG biosynthesis of both HSPGs and CS/DSPGs is initiated in the endoplasmic reticulum and Golgi apparatus by the formation of a common tetrasaccharide linkage region (glucuronic acid-galactose-galactose-xylose-*O*-) (GlcA-Gal-Gal-Xyl-*O*-) via *O*-glycosylation of a serine residue of the core protein (Fig. 1A) (1-3). The first step in the biosynthesis of this tetrasaccharide linkage region is catalyzed by xylosyltransferases (XylTs) encoded by the paralogues *XYLT1* [MIM 608124] and *XYLT2* [MIM 608125] (9). Two Gal residues are subsequently added by respectively galactosyltransferase I (GalT-I or β4GalT7 encoded by *B4GALT7* [MIM 604327]) and galactosyltransferase II (GalT-II or β3GalT6 encoded by *B3GALT6* [MIM 615291]) (10, 11). Further addition of a GlcA by glucuronosyltransferase I (GlcAT-I encoded by *B3GAT3)* [MIM 606374] completes the formation of the linkage region (12).

The cellular machinery required for GAG biosynthesis and modification is conserved over a broad range of eukaryotic organisms (13). The particular importance of a correct initiation of GAG synthesis is underscored by the identification of a series of severe, overlapping and multisystemic genetic human disorders that result from deficient activity of any of these ”linkage-enzymes”, collectively coined as ‘linkeropathies’ (14-16). The most frequently reported linkeropathy results from galactosyltransferase II deficiency, caused by biallelic pathogenic variants in *B3GALT6.* This leads to two clinically overlapping conditions, spondylodysplastic Ehlers-Danlos syndrome (EDS) (spEDS-*B3GALT6*) and

88 spondyloepimetaphyseal dysplasia with joint laxity type I (SEMD-JL1) (16, 17), both of which are
89 characterized by variable degrees of spondyloepimetaphyseal bone dysplasia, (with postnatal growth
90 restriction, bowing of long bones, hypo- or dysplasia of iliac and long bones, and vertebral body
91 changes), kyphoscoliosis, bone fragility with spontaneous fractures, joint hypermobility in conjunction
92 with joint contractures, hypotonia with delayed motor development, skin fragility, and craniofacial
93 dysmorphisms, including midfacial hypoplasia and dysplastic teeth (16-18). The severe and pleiotropic
94 phenotype suggests a critical role for *B3GALT6* in the development and homeostasis of various
95 connective tissues. Pathogenic variants in *B3GALT6* either result in mislocalization and/or reduced
96 amounts of active galactosyltransferase II (19). Previous studies on several biallelic *B3GALT6* variants
97 showed that they resulted in a barely detectable *in vitro* galactosyltransferase II enzymatic activity, but
98 intriguingly HS and CS/DS GAG synthesis was partially preserved *in cellulo* (20). While some variants
99 may have a greater deleterious effect on the *in vitro* than on the *in cellulo* enzymatic activity, it is
100 currently unknown whether there are rescue mechanisms at play to (partially) compensate for the
101 galactosyltransferase II activity.

102 In recent years, zebrafish have emerged as an excellent tool to model disease and to increase our
103 understanding of developmental processes and disease mechanisms. Zebrafish share 70% of their
104 genes with humans (21) and the advantages of their use are reflected by their large breed size, short
105 lifecycle and low husbandry costs (22). Zebrafish has proven to be a relevant genetic model for the
106 study of PG biosynthesis since many enzymes involved in this process are strongly conserved between
107 human and zebrafish (23), and a number of zebrafish models for defective PG synthesis (including
108 *fam20b*^{b1125}*, xylt1*^{b1189}*, or b3gat3*^{hi307}), provided novel knowledge on PG function in bone and cartilage
109 formation (23-26).

110 In this study, we generated *b3galt6* knock-out (KO) zebrafish as a model for spEDS-*B3GALT6* and SEMD-
111 JL1. These models were used to investigate the structure and amount of different GAG disaccharides
112 and the PG linkage region composition in these disorders. Furthermore, in-depth phenotypic
113 characterization of *b3galt6*$^{-/-}$ zebrafish was done to reveal to which extent key features of the human
114 disorders are recapitulated and to further elucidate the function of galactosyltransferase II in
115 vertebrate musculoskeletal development.

116

117 Results

118 CRISPR/Cas9-mediated *b3galt6* knock-out in zebrafish leads to reduced HS and CS/DS
119 glycosaminoglycan concentrations in bone, muscle and skin

120 Similar to its human orthologue, zebrafish *b3galt6* (NM_001045225.1) is a single-exon gene (Fig. 1B).
121 Human and zebrafish galactosyltransferase II (β3GalT6/B3galt6) protein sequence display 82.5 %
122 amino acid (AA) similarity, with the highest AA conservation in the luminal domain (Fig. 1C).

123 In order to investigate the consequences of zebrafish B3galt6-deficiency on GAG biosynthesis in
124 different tissues, we generated two *b3galt6* KO zebrafish models using CRISPR/Cas9 gene editing. The
125 first KO model carries the c.181delinsAAAGAGCTCCTAAAGGG indel mutation (cmg20 allele), leading
126 to a premature termination codon (PTC) (p.(Phe68*)), located upstream to the catalytic domain (Fig.
127 1D). RT-qPCR showed a 40.3% reduction of *b3galt6 mRNA* expression in homozygous adult *b3galt6* KO
128 zebrafish compared to wild-type (WT) siblings (Fig. 1E). For the remainder of this manuscript, this
129 model will be referred to as *b3galt6*$^{-/-}$. The second KO model carries a four base pair deletion
130 (c.398_401del) (cmg22 allele), predicted to generate a PTC (p.(Asn139*)) in the catalytic domain
131 (NM_001045225.1). This mutant was solely used for validation purposes (Fig. S1). Both *b3galt6* KO
132 zebrafish were produced at an expected Mendelian ratio and survived into adulthood. Unfortunately,
133 commercial antibodies, which were only available against human β3GalT6, did not work in our hands
134 and precluded the investigation of zebrafish B3galt6 protein levels and localization.

135

A

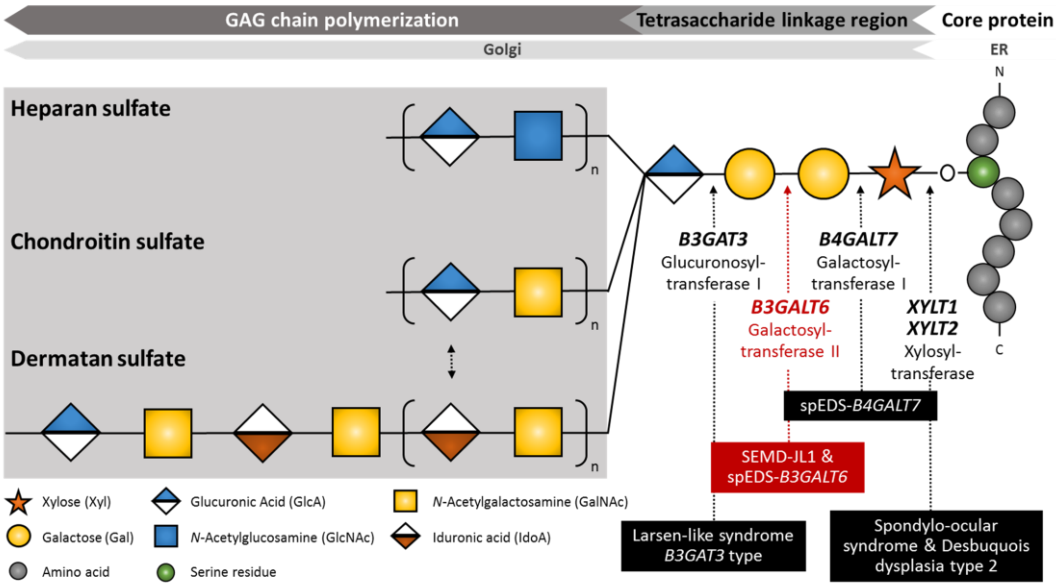

B

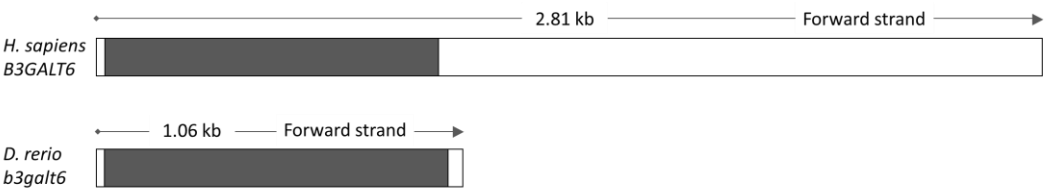

C

```
Q96L58 B3GT6_HUMAN     1   MKLLRRAWRRRAALGLGTLALCGAALLYLARCAAEPGDPRAMSGRSP-------PP---P    50
Q256Z7 Q256Z7_DANRE    1   MNLLRLVCRHKTALALGVLLLFAVVLLFLAKCTSETLKPAESPGAAPQAESHQKPPAGPA    60
                           *:*** . *:::**.**.* * ...**:**:*::*  .*    * :*       **

Q96L58 B3GT6_HUMAN    51   APARAAAFLAVLVASAPRAAERRSVIRSTWLARRGAPGDVWARFAVGTAGLGAEERRALE   110
Q256Z7 Q256Z7_DANRE   61   RPKELSAFLVILITTGPKYTERRSIIRSTWLTKHDPEVLY--WFVIGTEGLPAEDLQNLA   118
                            * . :***.:*::.*: :****:******:::.        *.:** ** **: : *

Q96L58 B3GT6_HUMAN   111   REQARHGDLLLLPALRDAYENLTAKVLAMLAWLDEHVAFEFVLKADDDSFARLDALLAEL   170
Q256Z7 Q256Z7_DANRE  119   TEQIRHHDLLLLPDLRDSYENLTQKLLHMYSWLDQNVEFKFVLKADDDTFARLDLLKEEL   178
                            ** ** ****** ***:***** *:* * :***::* *:********:***** *  **

Q96L58 B3GT6_HUMAN   171   RAREPARRRRLYWGFFSGRGRVKPGGRWREAAWQLCDYYLPYALGGGYVLSADLVHYLRL   230
Q256Z7 Q256Z7_DANRE  179   KVKEPK--ERLYWGFFSGRGRVKTAGKWKESAWELCDYYLPYALGGGYVLSADLVRYIRL   236
                           ::**   .************* .*:*:*:**:********************:*:**

Q96L58 B3GT6_HUMAN   231   SRDYLRAWHSEDVSLGAWLAPVDVQREHDPRFDTEYRSRGCSNQYLVTHKQSLEDMLEKH   290
Q256Z7 Q256Z7_DANRE  237   NVGFLKIWQSEDVSLGAWLAPVDVKRLHDPRFDTEYKSRGCSNKYLVTHKQSLEDMLEKH   296
                           . .:*: *:***************:* *********:******:***************

Q96L58 B3GT6_HUMAN   291   ATLAREGRLCKREVQLRLSYVYDWSAPPSQCCQRREGIP                       329
Q256Z7 Q256Z7_DANRE  297   QTLQRDGRLCKEEVKLRLSYIYDWSVPPSQCCQRKDGIP                       335
                            ** *:*****.**:*****:****.********::***
```

D

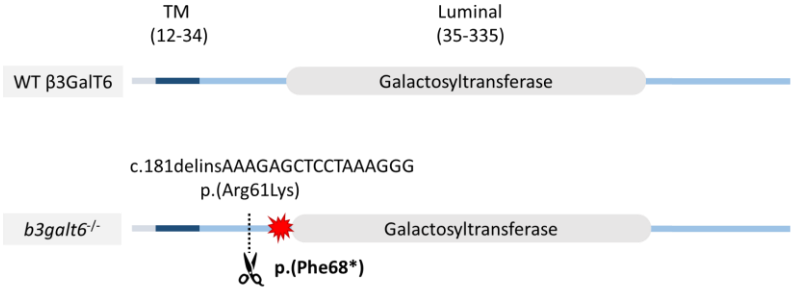

E

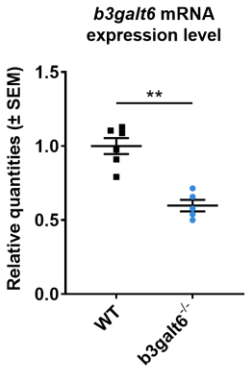

136

137 **Fig. 1. Schematic representation of the GAG biosynthesis and the evolutionary conservation of the zebrafish**
138 **and human *b3galt6/B3GALT6* gene and B3galt6/β3GalT6 protein.** (**A**) Simplified schematic representation of
139 the PG linkage and glycosaminoglycans biosynthesis. PG core proteins are synthesized in the endoplasmic
140 reticulum and undergo further modification in the Golgi apparatus. First, a tetrasaccharide linkage region is
141 synthesized that originates from the addition of a Xyl onto a serine residue of the core protein. Subsequent
142 addition of two Gals and one GlcA residues completes this process. Depending on the addition of GlcNAc or
143 GalNAc to the terminal GlcA residue of the linkage region, HS or CS/DS PGs will be formed, respectively. The
144 elongation of the GAG chain continues by repeated addition of uronic acid and amino sugar residues. The GAG
145 chain is then further modified by epimerization and sulfation (not shown). The main genes encoding for the
146 enzymes involved in the linkage region biosynthesis are indicated in bold and biallelic mutations in these genes
147 result in different linkeropathies. Disorders resulting from deficiency of the enzymes are indicated in black boxes.
148 The deficient enzyme (β3GalT6) and the related disorder studied here are depicted in red (e.g. spEDS-*B3GALT6*
149 and SEMD-JL1). (**B**) Schematic representation of the genomic structure of the *H. sapiens B3GALT6*
150 (NM_080605.4) and *D. rerio b3galt6* (NM_001045225.1) genes. The white and black boxes represent the
151 untranslated regions and the single *B3GALT6*/*b3galt6* exon, respectively. The zebrafish *b3galt6* gene resides on
152 chromosome 11, spans a region of 1.06 kb and has not been duplicated during teleost evolution. (**C**) Amino acid
153 (AA) sequence alignment (Clustal Omega) between *H. sapiens* β3GalT6 (Uniprot: Q96L58) and *D. rerio* B3galt6
154 (Uniprot: Q256Z7). The luminal galactosyltransferase domain is highlighted in grey. Conservation of AA
155 sequences is shown below the alignment: "*" residues identical in all sequences in the alignment; ":" conserved
156 substitutions; "." semi-conserved substitutions; "space" no conservation. (**D**) Schematic representation of the
157 cmg20 allele in *b3galt6* mutants. *b3galt6* consists of three parts, a cytosolic domain (AA 1-11), a transmembrane
158 domain (TM, AA 12-34) and a luminal domain (AA 35-335). The location of the CRISPR/Cas9-generated indel
159 variant is indicated by a scissor symbol and the resulting premature termination codon (PTC) is depicted by a red
160 star. (**E**) RT-qPCR analysis of relative *b3galt6* mRNA expression levels in *b3galt6*$^{-/-}$ adult zebrafish (0.597 ±
161 0.03919) (n=5) compared to WT siblings (1 ± 0.05395) (n=6). Data are expressed as mean ± SEM. A Mann-Whitney
162 U test was used to determine significance, **P<0.01.

163 To examine the activity of B3galt6 in different *b3galt6*$^{-/-}$ tissues, concentrations of CS, DS and HS
164 disaccharides extracted from bone, muscle and skin from WT and *b3galt6*$^{-/-}$ zebrafish were quantified
165 using a combination of enzymatic digestion and anion-exchange HPLC (Figs. S2-S5 and Tables S1-S4).
166 Overall, a generalized decrease in HS, CS and DS concentration was detected in all examined tissues of
167 *b3galt6*$^{-/-}$ zebrafish. In the GAG fractions prepared from bone, the disaccharide concentration of the
168 CS/DS and CS moieties was significantly decreased by respectively 55% and 64%, compared to WT
169 zebrafish (Table 1 and Tables S1 and S2). DS moieties were undetectable in bone of *b3galt6*$^{-/-}$ zebrafish,
170 whereas their concentration was 50.5 pmol/mg protein in bone of WT zebrafish (Table 1 and Table

171 S3). A non-significant decrease in the disaccharide concentration of the HS moiety was observed in
172 *b3galt6*$^{-/-}$ mutant bone (Table 1 and Table S4), compared to WT. In GAG fractions prepared from
173 *b3galt6*$^{-/-}$ muscle, CS/DS, CS and DS disaccharide moieties were generally lower than in WT muscle
174 (Table 1 and Tables S1-S3). Due to the low concentrations close to the detection limit, a significant
175 reduction could only be detected for the DS moiety (72% reduction) (Table 1 and Table S3). In addition,
176 a significant decrease in HS disaccharide moieties by 56% was noted in *b3galt6*$^{-/-}$ muscle compared to
177 WT muscle (Table 1 and Table S4). In the GAG fractions prepared from *b3galt6*$^{-/-}$ skin, the concentration
178 of all disaccharide moieties was significantly reduced compared to WT (Table 1 and Tables S1-S4). The
179 disaccharide concentration of the CS/DS, CS, DS and HS moieties were decreased by respectively 77%,
180 73%, 55% and 62% compared to WT (Table 1 and Tables S1-S4). No altered sulfation patterns were
181 observed in disaccharide moieties when comparing unique GAG chains between WT and *b3galt6*$^{-/-}$
182 zebrafish samples (Tables S1-S4).

183 Despite the strong reduction in disaccharide concentrations observed in *b3galt6*$^{-/-}$ zebrafish, low
184 amounts of GAGs were still produced in the mutants. Similar results were obtained for the second
185 *b3galt6* KO zebrafish (cmg22 allele) (Table S5). RT-qPCR revealed no significant upregulation of other
186 galactosyltransferase(s) member(s) from the *b3galt* family (*b3galt1a*, *b3galt2*, *b3galt4*, *b3galnt2*) or of
187 other linkage-enzymes (*xylt1*, *xylt2*, *b4galt7* and *b3gat3*) (Fig. S6), suggesting that altered expression
188 of these genes did not compensate for the reduced *b3galt6* mRNA levels.

189 **Table 1. Concentrations of GAG disaccharides in wild-type and *b3galt6*$^{-/-}$ zebrafish tissues**

	pmol/mg protein (Average ± SE)			
	CS/DS	CS	DS	HS
Bone				
Wild-type	774.2 ± 19.9	728.4 ± 148.1	50.5 ± 8.1	178.6 ± 19.8
b3galt6$^{-/-}$	346.1 ± 20.0*	279.9 ± 4.8**	N.D.	137.1 ± 39.7^{ns}
Muscle				
Wild-type	9.3 ± 0.4	2.1 ± 0.4	14.5 ± 1.1	30.8 ± 1.2
b3galt6$^{-/-}$	5.7 ± 3.1^{ns}	N.D.	4.1 ± 1.0*	13.5 ± 4.0**
Skin				
Wild-type	236.2 ± 26.5	175.1 ± 25.3	75.9 ± 7.9	55.1 ± 4.5
b3galt6$^{-/-}$	55.4 ± 15.2*	47.9 ± 13.5**	33.8 ± 6.3**	21.0 ± 2.8**

190 Student's t-test (vs wild-type) (n=3), N.D.: not detected (<1 pmol/mg protein), *P<0.01, **P<0.05, ns: not
191 significant, SE: standard error.

192 **B3galt6-deficiency leads to the biosynthesis of a non-canonical (GlcA-Gal-Xyl-*O*-) trisaccharide**
193 **linkage region in zebrafish**

194 In order to explain why *b3galt6*$^{-/-}$ zebrafish can still produce GAG chains on PG core proteins, we
195 investigated the composition of the linkage region. To this purpose, whole zebrafish extracts were
196 enriched for all proteoglycans, their GAG chains depolymerized with bacterial lyases, the core proteins
197 digested with trypsin and the remaining glycopeptides subjected to nano-scale liquid chromatography-
198 tandem mass spectrometry (nLC-MS/MS) using a recently developed glycoproteomic approach (27,
199 28). Potential structural differences in PG linkage regions in WT versus *b3galt6*$^{-/-}$ zebrafish are thus
200 elucidated through the combined identities of peptide backbones and GAG linkage region structures.
201 The glycoproteomic analysis identified two CS-glycopeptides derived from biglycan (UniProt: A8BBH0)
202 in both the WT and *b3galt6*$^{-/-}$ zebrafish. These CS-glycopeptides displayed different linkage region
203 structures in WT compared with *b3galt6*$^{-/-}$ zebrafish (Fig. 2). While the peptide in the WT zebrafish was
204 modified with a hexasaccharide structure (Fig. 2A), the peptide in the *b3galt6*$^{-/-}$ zebrafish was modified
205 with a pentasaccharide structure (Fig. 2B), supporting the hypothesis that *b3galt6*$^{-/-}$ zebrafish produces
206 a non-canonical trisaccharide linkage region. The precursor ion (m/z 1281.7922; 3+) in the WT
207 zebrafish equated to a mass of a peptide (DQEEGSAVEPYKPEHPTCPFGCR) modified with a
208 hexasaccharide structure, with the peptide containing two carbamidomethyl (CAM) modifications.
209 Furthermore, the hexasaccharide structure was modified with one sulfate group (SO_3^-) on the
210 subterminal GalNAc residue [GlcAGalNAc-H_2O+SO_3+H]$^+$, and one phosphate group (HPO_3^-) on the Xyl
211 residue (Fig. S7). In contrast, the precursor ion (*m/z* 1227.7765; 3+) in the *b3galt6*$^{-/-}$ zebrafish equated
212 to a mass of the same peptide but modified with a pentasaccharide structure, with two
213 phosphate/sulfate groups, with the peptide containing two CAM modifications. The difference in mass
214 between the WT and *b3galt6*$^{-/-}$ precursor ions corresponds to 162.08 Da, equating to the mass of a
215 hexose (galactose) residue (162 Da). Additional HS- and CS- glycopeptides with the expected
216 tetrasaccharide linkage region were found in the WT. In the *b3galt6*$^{-/-}$, no HS-modified structures were
217 identified but additional CS-glycopeptides with the non-canonical trisaccharide linkage region were
218 found. Table S6 shows a complete list of all glycopeptides identified in both WT and *b3galt6*$^{-/-}$ zebrafish.
219 PGs harboring a tetrasaccharide linkage region were never detected in the *b3galt6*$^{-/-}$ adult zebrafish
220 samples and no trisaccharide linkage region was detected in WT zebrafish samples.

221 These observations suggest that B3GAT3/GlcAT-I can transfer a GlcA residue not only to Gal-Gal-Xyl,
222 but also to a Gal-Xyl substrate. This was confirmed by an *in vitro* GlcAT-I assay, which showed that
223 GlcAT-I is indeed capable of adding a GlcA to a Gal-Xyl-*p*-nitrophynyl, which was chemically
224 synthesized, thus to a substrate ending with a single galactose (Fig. S8).

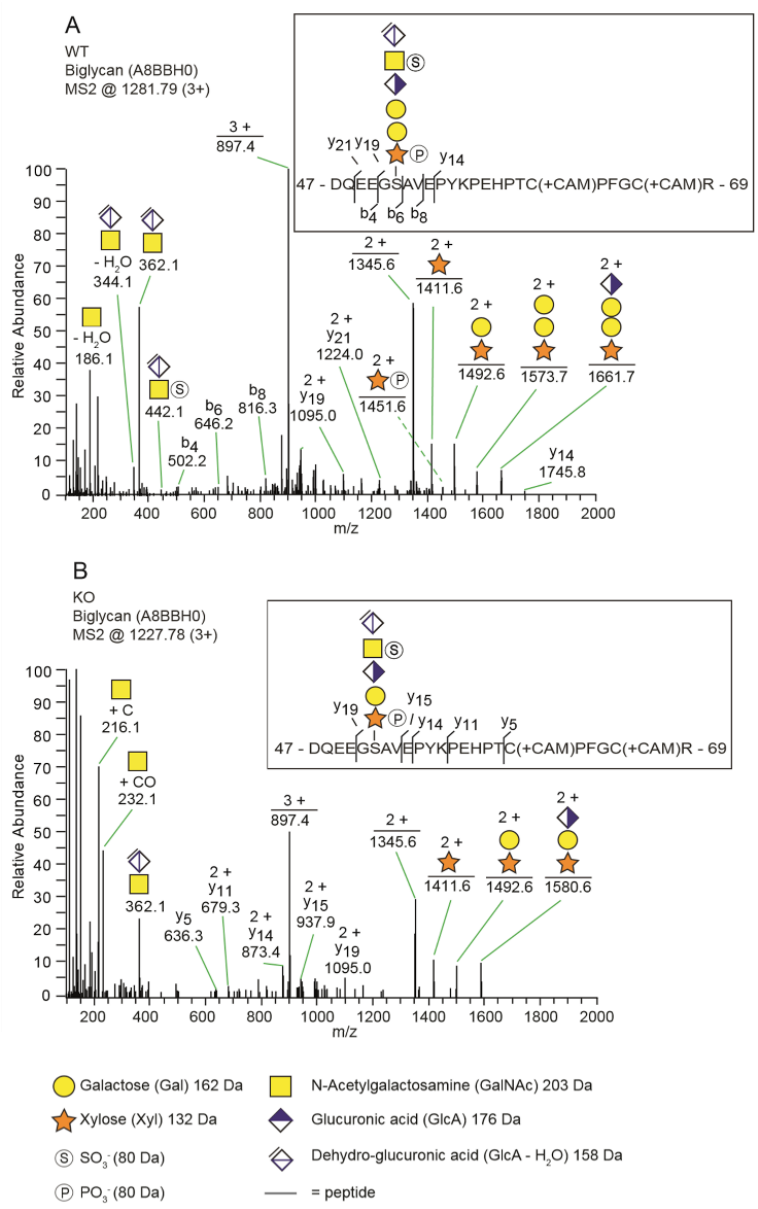

Fig. 2. The identification of a trisaccharide linkage region in the *b3galt6*$^{-/-}$ zebrafish. (**A** and **B**) MS2 fragment mass spectra of CS-glycopeptides derived from biglycan (UniProt: A8BBH0) showed different linkage regions in WT compared to the *b3galt6*$^{-/-}$ zebrafish. (**A**) The peptide (DQEEGSAVEPYKPEHPTCPFGCR) in WT zebrafish was modified with a residual hexasaccharide structure, corresponding to the canonical tetrasaccharide linkage region (*m/z* 1281.79; 3+). The hexasaccharide structure was modified with one sulfate group (SO_3^-) at the subterminal GalNAc residue and one phosphate group (HPO_3^-) at the xylose residue (Fig. S7) (**B**) The peptide (DQEEGSAVEPYKPEHPTCPFGCR) in *b3galt6*$^{-/-}$ zebrafish was modified with a residual pentasaccharide structure, corresponding to a non-canonical trisaccharide linkage region (*m/z* 1227.78; 3+). The pentasaccharide structure was modified with two phosphate/sulfate groups. Their exact positioning and identity could not be determined due to low intensities of corresponding ion peaks, and the positions are therefore assigned in analogy of the WT structure.

237

238 ***b3galt6*$^{-/-}$ zebrafish show early-onset, progressive morphological abnormalities and delay of**
239 **cartilage and bone formation, reminiscent of human spEDS-*B3GALT6***

240 One of the clinical hallmarks of human spEDS-*B3GALT6* is the pronounced skeletal involvement with
241 the presence of spondyloepimetaphyseal dysplasia with postnatal growth restriction, bowing of long
242 bones, hypoplasia of iliac bones, femoral head dysplasia, vertebral body changes, kyphoscoliosis and
243 bone fragility with spontaneous fractures (Table 2). To evaluate the development of cartilage and bone
244 associated with B3galt6-deficiency in zebrafish, phenotypic characterization of *b3galt6*$^{-/-}$ zebrafish was
245 performed in juvenile (20 dpf, days post fertilization) and adult stages (four months).

246 At 20 dpf, the average weight (W), standard length (SL) and Fulton's condition factor (*K*), which is used
247 as a measure for the relative proportion of SL to W (29), were not significantly different between
248 *b3galt6*$^{-/-}$ and WT siblings (Fig. 3A), although for SL there was a trend towards smaller mutants
249 (P=0.0640). Several externally visible morphological anomalies could be observed in 20 dpf *b3galt6*$^{-/-}$
250 zebrafish as compared to their WT siblings, including a shorter, more compact head, a shorter and
251 rounder frontal region, a shorter parietal/occipital region and a malformed posterior edge of the
252 opercular apparatus (Fig. 3B). Alcian blue (AB) cartilage staining showed no morphological
253 abnormalities, but developmental delay of the head and pectoral and caudal fin endoskeleton was
254 noted (Fig. 3B, Table S7), with cartilage elements being absent or in early development in *b3galt6* KO,
255 while these structures were already fully developed in WT sibling zebrafish. Alizarin red (AR) mineral
256 staining showed delayed mineralization in all regions of the head, the pectoral fin girdle and the caudal
257 fin (Fig. 3B, Table S8), further confirming developmental retardation. In addition, malformations of
258 different mineralized bones, such as the parasphenoid, branchiostegal rays, supracleithrum and the
259 subopercle bone could be detected in the head of *b3galt6*$^{-/-}$ zebrafish larvae (Fig. S9). The vertebral
260 column, i.e. the vertebral centra and their associated elements (neural and haemal arches), did not
261 show delayed mineralization in *b3galt6*$^{-/-}$ zebrafish larvae, but malformation of the associated
262 elements and fusions of preural vertebrae were observed at a much higher frequency in the *b3galt6*$^{-/-}$
263 mutants. Kyphosis, scoliosis and lordosis were also more frequently observed and pronounced in
264 *b3galt6*$^{-/-}$ larvae compared to WT siblings (Fig. S10 & Table S8). A similar phenotype was observed in
265 the second *b3galt6* KO model (cmg22 allele), confirming the specificity of the displayed phenotype
266 (Fig. S11).

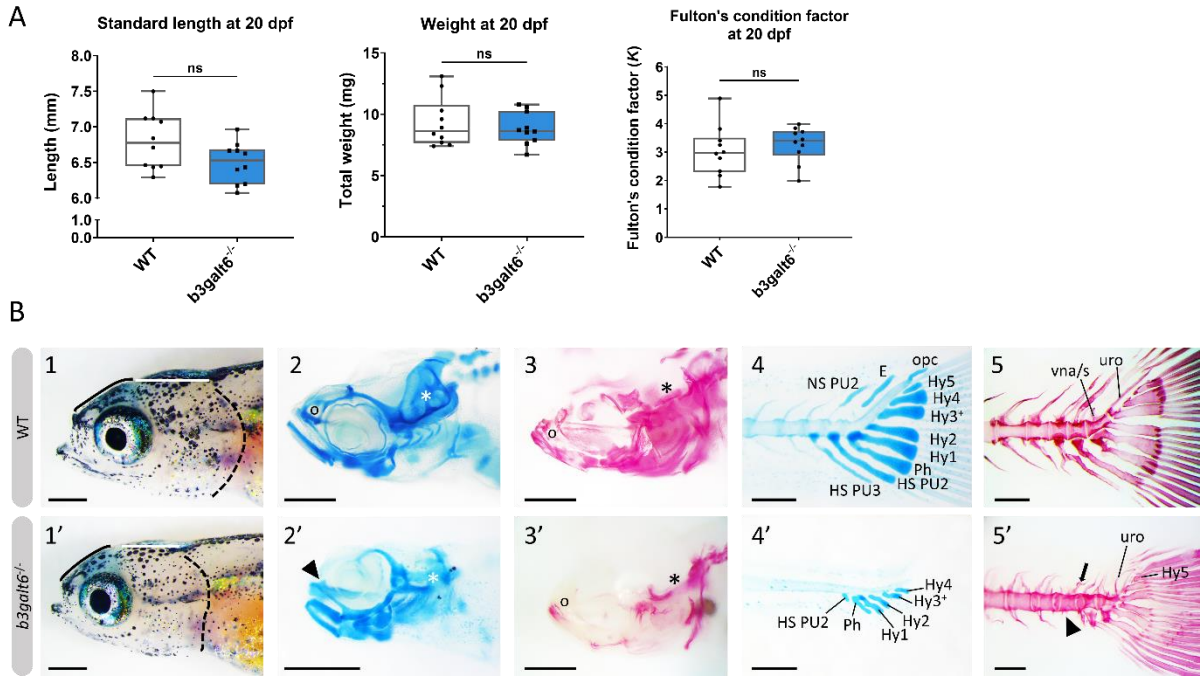

Fig. 3. Developmental delay and morphological abnormalities in 20 dpf *b3galt6*$^{-/-}$ zebrafish. (**A**) Weight, standard length and Fulton's condition factor of WT and *b3galt6*$^{-/-}$ zebrafish larvae at 20 dpf (n=10). (**B**) External phenotype of the head of juvenile WT and *b3galt6*$^{-/-}$ sibling zebrafish. All images are oriented anterior to the left, posterior to the right, dorsal to the top and ventral to the bottom. (**1-1'**) *b3galt6*$^{-/-}$ zebrafish display a rounder frontal region (black line), shorter parietal/occipital region (white horizontal line) and a malformed posterior edge of the opercular apparatus (dotted black line), compared to WT control. (**2-2'**) Representative images of cartilage AB staining of the head. The olfactory region (indicated by 'o' in the WT and arrowhead in the *b3galt6*$^{-/-}$ picture) and the otic region (indicated by white asterisk) show delayed development of cartilage elements in *b3galt6*$^{-/-}$ zebrafish as compared to WT. (**3-3'**) Representative images of AR mineral staining of the head. The olfactory region (indicated by 'o') and the otic region (indicated by asterisk) show severely delayed mineralization in *b3galt6*$^{-/-}$ zebrafish larvae as compared to WT. (**4-4'**) Representative images of AB staining of the caudal fin. The modified associated elements show developmental delay in *b3galt6*$^{-/-}$ zebrafish as compared to WT. Abbreviations: E, epural; HS PU2, haemal spine of preural 2; HS PU3, haemal spine of preural 3; Hy1-5, hypural 1-5; NS PU2, neural spine preural 2; opc, opistural cartilage; Ph, parhypural (**5-5'**) Representative images of AR mineral staining of the caudal fin. Caudal vertebrae and their associated elements show no delay in ossification. Malformation or absence of caudal fin associated elements (block arrow indicates a neural arch; arrowhead indicates a missing haemal arch), and malformation of uroneural (uro) and vestigial neural arches and spines (vna/s) are observed in *b3galt6*$^{-/-}$ zebrafish; hypurals have a bent appearance. Scale bars: images of the head 500 µm, images of the caudal fin 200 µm.

288 At the adult stage (four months), *b3galt6*$^{-/-}$ zebrafish had a significantly reduced average SL (1.834 ±
289 0.077 cm), and W (0.1196 ± 0.014 g), when compared to their WT siblings (2.371 ± 0.049 cm, and
290 0.2497 ± 0.016 g, respectively), while the Fulton's condition factor (*K*) indicated that SL and W were
291 normally proportioned to each other (Fig. 4A). A similar phenotype was observed in the second *b3galt6*
292 KO model (cmg22 allele), confirming the specificity of the displayed phenotype (Fig. S1).

293 The head malformations, which were already observed in 20 dpf *b3galt6*$^{-/-}$zebrafish, showed further
294 progression, with a more pronounced smaller, rounded head and an abnormal compaction of the
295 opercular apparatus (Fig. 4B). In addition, a reduced surface area of the fins, with a crenelated postero-
296 distal fin edge was observed in the mutant animals. The pectoral fins were pointing in an abnormal
297 upwards angle (Fig. 4B). Kyphoscoliosis was variably present and mainly occurred in the posterior part
298 of the body (not shown). In addition, an altered pigmentation pattern was observed, mainly on the
299 ventral part of the body where the dark stripes showed interruptions (Fig. 4B).

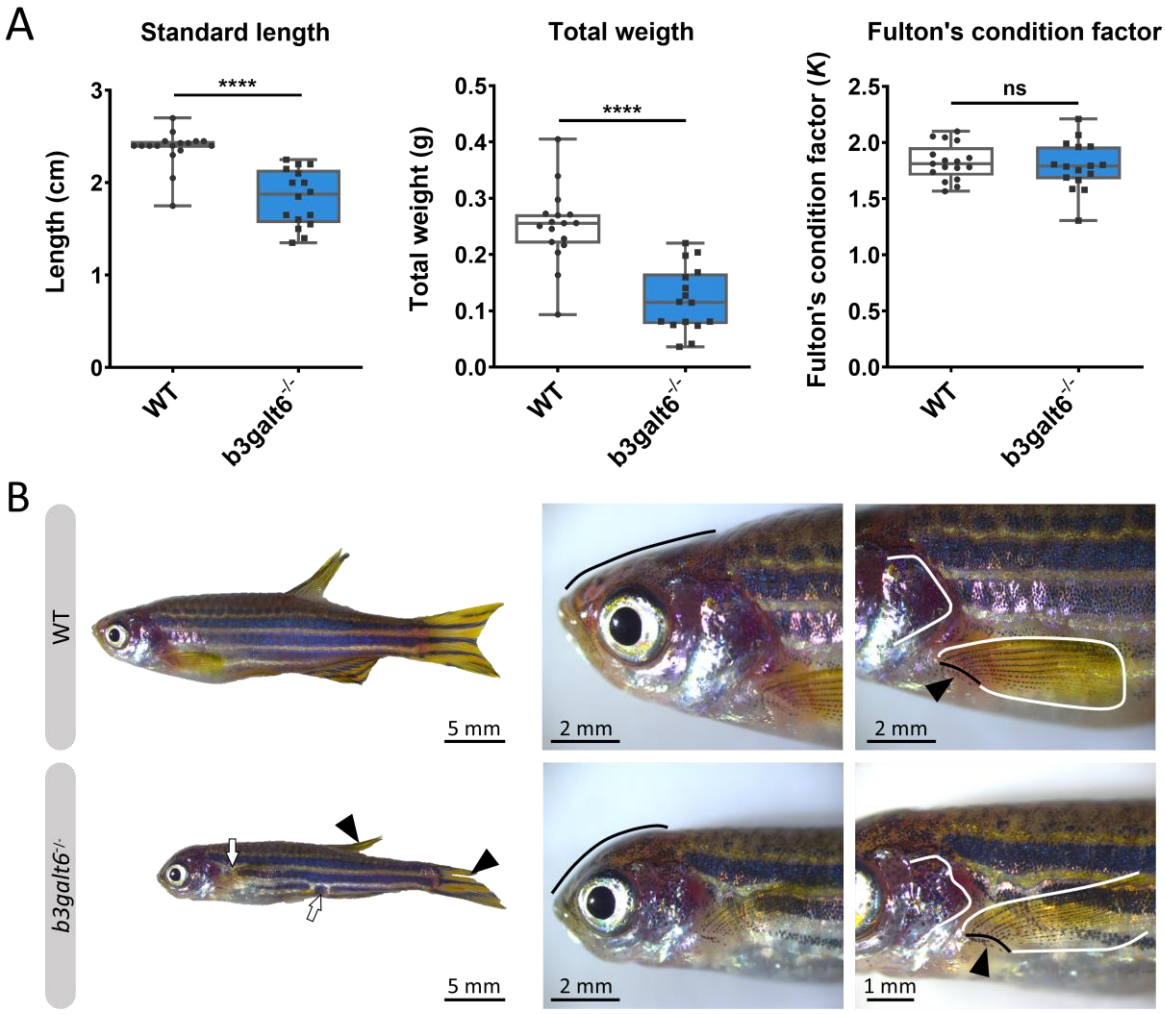

300

301 **Fig. 4. Characterization of the external phenotype of adult *b3galt6*$^{-/-}$ zebrafish.** (**A**) *b3galt6*$^{-/-}$ zebrafish (n=16)
302 had a significantly shorter standard length (SL) compared to their WT siblings (n=17). The weight (W) was
303 significantly lower in the mutant zebrafish. The Fulton's condition factor (K= 100*(W/SL^3)) was not significantly
304 different between *b3galt6*$^{-/-}$ zebrafish and WT siblings. Data are expressed as box plots with min-to-max whiskers
305 on which each individual data point is plotted. An unpaired t-test with Welch's correction was used to determine
306 significance. ****P<0.0001, ns: not significant. (**B**) Adult *b3galt6*$^{-/-}$ zebrafish exhibit morphological abnormalities
307 compared to their WT siblings; *b3galt6*$^{-/-}$ zebrafish display interruptions of the blue horizontal stripes (white
308 arrows), smaller fins (arrowhead), aberrations of the head shape (black line), of the shape of the opercular
309 apparatus (white line indicates the posterior edge) and of the pectoral fin (black line and arrow indicate the fin
310 rays at the base of the fin, white line shows the outline of the fin).

311 Further progression of the larval phenotype was also confirmed by AR staining of the mineralized
312 skeleton in adult (four months) *b3galt6*$^{-/-}$ zebrafish. The olfactory region was underdeveloped (Fig. 5A),
313 the cranial roof bones and sutures were deformed (Fig. S12) and the opercular apparatus was smaller
314 and compacted in KO zebrafish (Fig. 5A and Fig. S12). The fifth ceratobranchial arch and its attached
315 teeth were smaller in *b3galt6*$^{-/-}$ zebrafish (Fig. 5B). In the pectoral fins of *b3galt6*$^{-/-}$ zebrafish the radials
316 were smaller, had an irregular shape, and were often fused (Fig. 5B). The autocentra, i.e. the inner
317 layer of the vertebral centra in the vertebral column and caudal fin (30) of KO zebrafish had a normal
318 hourglass shape, but the associated elements often showed presence of extra intramembranous bone
319 (Fig. 5 and Fig. S12) and extra bony elements (Fig. 5A). Fusions were observed in preural vertebrae (Fig.
320 5A). Lordosis, kyphosis and scoliosis was variably observed along the vertebral column of *b3galt6*$^{-/-}$
321 mutant zebrafish (not shown). Extra mineralization was observed at the edge (growth zone) of *b3galt6*$^{-}$
322 $^{/-}$ scales (Fig. 5B). Notably, variation in the severity of the skeletal malformations in *b3galt6*$^{-/-}$ zebrafish
323 was observed.

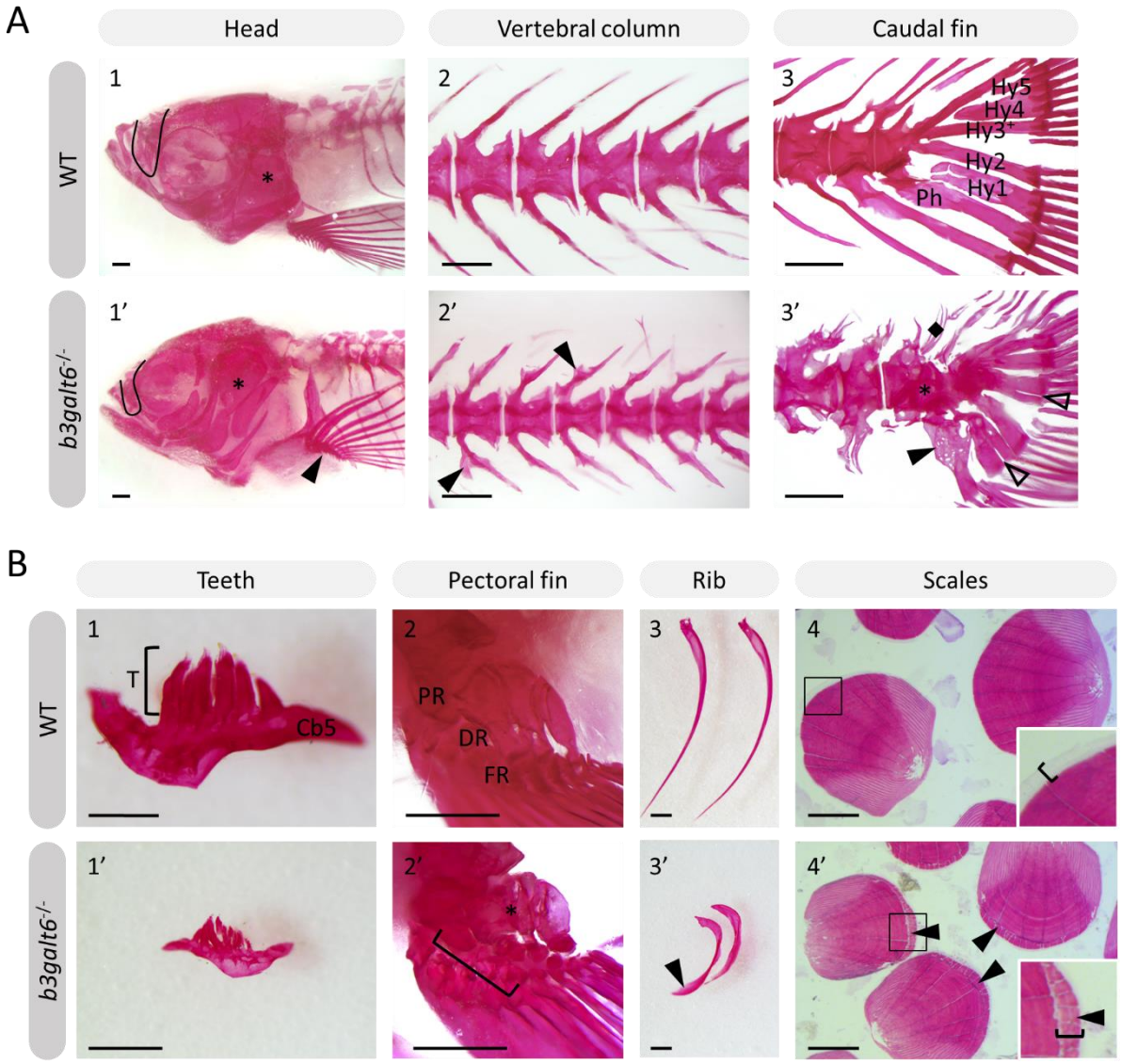

Fig. 5. Alizarin red stained mineralized bone in WT and *b3galt6*$^{-/-}$ adult zebrafish. The mineralized bones in the skeleton were studied in four-month-old WT and mutant zebrafish after AR mineral staining. (**A**) *b3galt6*$^{-/-}$ zebrafish display malformation of the cranium, vertebral column and caudal fin. (**A1-1'**) The cranium shows an underdeveloped olfactory region (black line) and a smaller compacted opercular bone (asterisk). (**A2-2'**) The vertebral column shows extra intramembranous outgrowths located where the distal tip of the neural and haemal arches fuse to neural and haemal spine respectively (arrowheads). (**A3-3'**) In the caudal fin fusion of preural vertebrae is observed (asterisk). Associated elements show intramembranous outgrowths (arrowhead) and the presence of extra bony elements (diamond). The distal tip of the hypurals is sometimes split (transparent arrowhead). Structures indicated in the WT caudal fin: Hy1-5, hypural 1-5, Ph, parhypural. (**B**) Details of mineralized structures in *b3galt6*$^{-/-}$ zebrafish. (**B1-1'**) The fifth ceratobranchial arch and its teeth are smaller in KO zebrafish. (**B2-2'**) The proximal (PR) and distal radials (DR) have irregular shapes in mutant zebrafish. Proximal (asterisk) and distal radials are sometimes fused. The bracket indicates a fusion between a proximal and distal

337 radial, and the first fin ray (FR). (**B3-3'**) Ribs also show extra intramembranous bone (black arrowhead). (**B4-4'**)
338 More mineralization was observed at the growth zone (bracket) of the scales in mutant zebrafish (arrowhead).
339 Scale bars = 500 µm.

340 Subsequent quantitative µCT analysis of four-month-old zebrafish revealed multifaceted effects of
341 B3galt6-deficiency on vertebral morphology and mineralization. Most notably, the volume of vertebral
342 centrum, haemal and neural associated elements was significantly reduced throughout the entire
343 vertebral column in *b3galt6*$^{-/-}$ zebrafish (P<0.01), with more pronounced differences in the abdominal
344 region (Fig. 6). Tissue mineral density (TMD) was not significantly different in the *b3galt6*$^{-/-}$ vertebral
345 bodies compared to WT siblings. However, TMD in zebrafish is proportionally related to standard
346 length (31, 32), and *b3galt6*$^{-/-}$ zebrafish exhibited a significantly reduced body size compared to the
347 WT siblings. We therefore normalized the µCT data to standard length using the normalization
348 procedure outlined by Hur *et al.* (33). In this procedure, phenotypic data in WT sibling controls was
349 scaled using the mean standard length of *b3galt6*$^{-/-}$ zebrafish as the reference length. Remarkably,
350 after normalization, a significant increase in TMD of centrum, haemal and neural associated elements
351 was noted in *b3galt6*$^{-/-}$ zebrafish compared to WT controls (P<0.001, P<0.01 and P<0.01, respectively)
352 (Fig. S13).

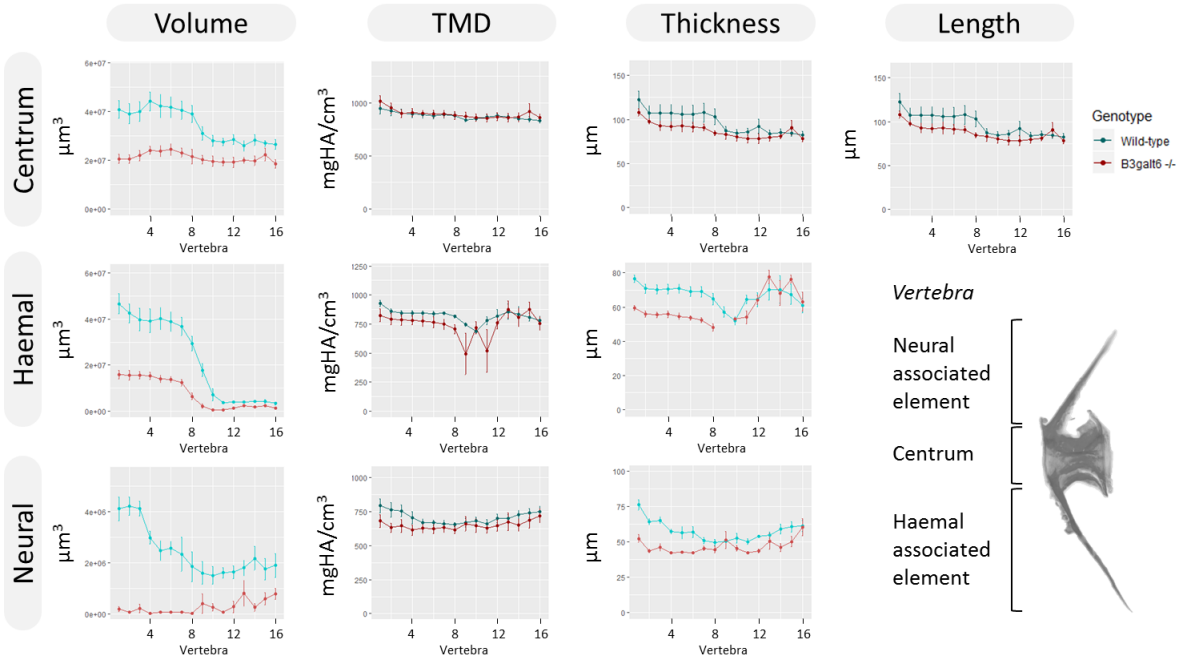

353

354 **Fig. 6. µCT analysis of adult WT and *b3galt6*$^{-/-}$ zebrafish.** Quantitative µCT analysis of the vertebral column in
355 five mutant versus five WT zebrafish at the age of four months. The bone volume, tissue mineral density (TMD)
356 and bone thickness were calculated for three parts of each vertebra: the vertebral centrum, the neural associated

357 element (neural arch and neural spine) and the haemal associated element (haemal arch and haemal spine).
358 Plots associated with a significant difference are colored in a lighter coloring scheme. The X-axis represents each
359 vertebra along the anterior-posterior axis. The volume is significantly reduced for each part of the vertebra in
360 *b3galt6*$^{-/-}$ zebrafish (P<0.01, P<0.001 and P<0.000001, respectively). The thickness of the haemal (P<0.01) and
361 neural (P=0.001) associated element is also significantly reduced in the mutants whereas the centrum thickness
362 is not significantly reduced in *b3galt6*$^{-/-}$ zebrafish (P=0.12). TMD is not significantly different between *b3galt6*$^{-/-}$
363 zebrafish and WT siblings when not normalized for standard length (P>0.2). Data are presented as mean ± SEM.
364 TMD, tissue mineral density; HA, hydroxyapatite.

365 ***b3galt6* knock-out zebrafish display a disturbed organization of type I collagen fibrils in skin, bone**
366 **and intervertebral space**

367 Transmission electron microscopy (TEM) studies on the dermis of spEDS-*B3GALT6* patients revealed
368 an abnormal collagen fibril architecture with loosely packed collagen fibrils of variable size and shape
369 (5). We therefore studied the effect of loss of galactosyltransferase II activity on collagen fibril
370 architecture. TEM sections of skin biopsies of *b3galt6*$^{-/-}$ zebrafish showed an abnormal dermal collagen
371 fibril architecture characterized by loosely packed collagen fibrils and larger and more interfibrillar
372 spaces compared to WT siblings (Fig. 7A). In addition, at the level of the scales a thicker epidermal
373 layer was observed and electron dense structures were present in the interfibrillar spaces (Fig. 7A).
374 Next, we examined the intervertebral region and adjacent vertebral centra in the vertebral column of
375 five-month-old zebrafish by means of TEM. In general, the type I collagen fibers in *b3galt6*$^{-/-}$ zebrafish
376 displayed a lower degree of organization (Fig. 7B). This was observed in immature collagen layers,
377 deposited by osteoblasts in the outer edges of the intervertebral space, but also in the mature type I
378 collagen layers of the intervertebral ligament and in the autocentrum, the inner layer of the vertebral
379 bone, where a lack of the typical plywood-like organization was seen. Detailed investigation of TEM
380 sections of the vertebral bone revealed presence of several electron dense spots of unknown origin in
381 knock-outs. These 'dark spots' may reflect extrafibrillar hydroxyapatite crystals (Fig. 7B).

382 Mass spectrometry analysis of type I collagen modification in bone derived from the vertebral column
383 showed no significant difference in hydroxylation status of the α1(I) K87 and C-telopeptide lysine
384 residues (Table S9). These lysine residues are conserved in zebrafish and human type I collagen and
385 are crucial for intermolecular crosslinking of collagen fibrils in bone matrix (34).

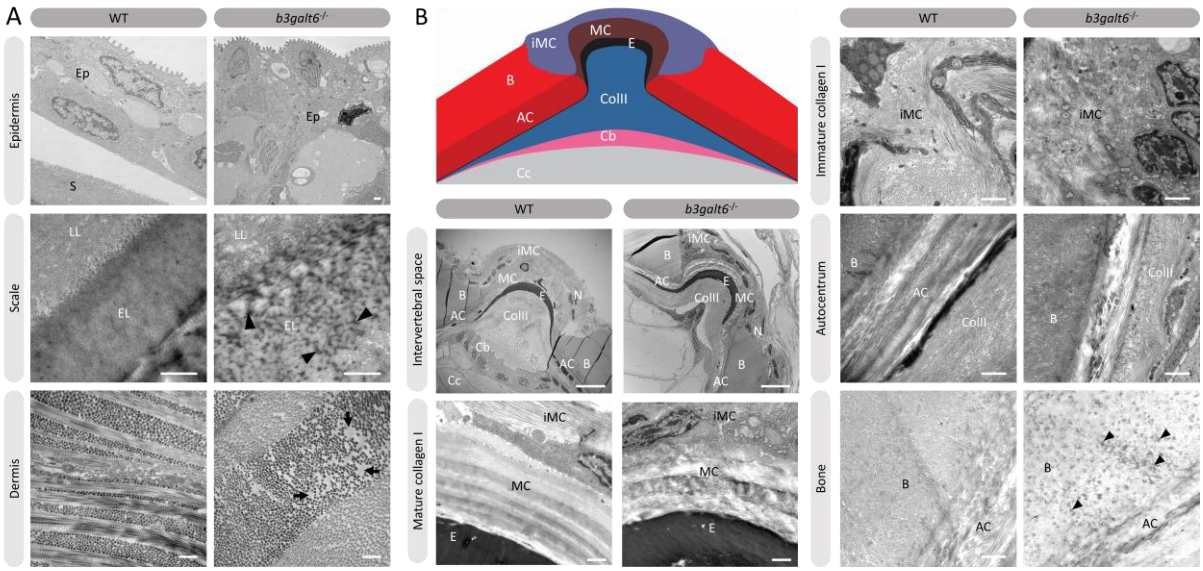

Fig. 7. Collagen fibrillar architecture in five-month-old adult zebrafish. (**A**) Skin from five-month-old WT and *b3galt6*$^{-/-}$ adult zebrafish. The epidermis (Ep), the outer layer of the skin covering the scales (S) of zebrafish, appears thicker in *b3galt6*$^{-/-}$ zebrafish compared to the epidermis of WT zebrafish. A mature zebrafish scale consists of several layers. The limiting layer of the scale (LL) is rich in fine granules that in some areas are linearly arranged, forming dense layers. This matrix contrasts with that of the external layer(s) (EL) below. Structures resembling extrafibrillar crystals (arrowhead) are noted in the external layer of the mutant scale, which are rare in WT zebrafish sections. Upon investigation of the dermis of *b3galt6*$^{-/-}$ mutants, increased interfibrillar spaces are noted (arrows), which are absent in the dermis of WT adults. Scale bars = 500 nm. (**B**) Schematic representation and TEM images of the zebrafish intervertebral space. Schematic representation of the zebrafish intervertebral space. Abbreviations: AC, autocentrum; B, bone; Cb, chordoblasts; Cc, chordocytes; ColII, type II collagen; E, elastin; iMC, immature collagen type I layer; MC, mature collagen type I layer. Starting from the central body axis, several recognizable structures are present in the intervertebral space along a proximo-distal axis: (i) notochord tissue consisting of chordocytes and chordoblasts, (ii) the notochord sheath consisting of a type II collagen layer and an external elastic membrane, (iii) and a connective tissue ligament consistent of a mature and an immature type I collagen layer. The mature type I collagen layer is organized in a typical plywood-like pattern and is continuous with the inner layer of the vertebral bone, i.e. the autocentrum, which also shows a plywood-like organization. The immature type I collagen layers consist of loose collagen fibers connecting the outer layer of vertebral bones. Notice the higher number of nuclei (N) in the *b3galt6*$^{-/-}$ zebrafish at the intervertebral space. Mature collagen (MC) displays a typical plywood-like organization, in WT zebrafish but not in comparable regions for *b3galt6*$^{-/-}$ mutant zebrafish. Cross section and longitudinal type I collagen regions are less clearly demarcated and smaller in immature collagen (iMC) from *b3galt6*$^{-/-}$ zebrafish compared to WT siblings. It is more difficult to pinpoint the different layers of the autocentrum (AC) in the KO compared to WT

409 zebrafish. Bone (B) from the *b3galt6*$^{-/-}$ zebrafish shows electron dense structures (arrowhead). Scale bars = 10
410 µm for the intervertebral space and 1 µm for the other images.

411 ***b3galt6* knock-out zebrafish display ultrastructural muscle abnormalities and lower endurance**

412 Human spEDS-*B3GALT6* patients often suffer from muscle hypotonia with a delay in motor
413 development. In view of the observed reduction in the concentration of the different GAG moieties in
414 muscle of *b3galt6*$^{-/-}$ zebrafish, we investigated the function and the ultrastructural appearance of
415 muscle.

416 First, the critical swimming speed (U_{crit}) and endurance of the zebrafish were assessed by means of a
417 custom-made swim tunnel. The U_{crit}, defined as the maximum velocity that the tested zebrafish could
418 sustain for at least 5 minutes (35), was significantly lower in *b3galt6*$^{-/-}$ zebrafish (30.1 ± 2.39 cm/s)
419 compared to length-matched WT (41.61 ± 1.942cm/s) ($P<0.01$) (Fig. 8A). The stamina of each zebrafish
420 was determined by an effort test where it was tested how long zebrafish could swim at high speed (37
421 cm/s) after a three-minute warm-up. This effort test showed that the *b3galt6*$^{-/-}$ zebrafish performed
422 less well compared to length-matched WT zebrafish, indicating a lower endurance (Fig. 8B).

423 The muscle tissue in the zebrafish trunk was further investigated at the ultrastructural level. Toluidine
424 blue-stained semi-thin cross sections revealed that the endomysium, a layer of connective tissue
425 ensheating the muscle fibers, was enlarged along the horizontal myoseptum of *b3galt6*$^{-/-}$ zebrafish,
426 although no clear differences in muscle fiber diameter were noted (Fig. 8C). Ultra-thin parasaggital
427 sections, investigated by TEM, showed that the length of the sarcomeres, the smallest basic units of
428 striated muscle, as well as the length of the A and I band were significantly increased in the *b3galt6*$^{-/-}$
429 zebrafish (Fig. 8D).

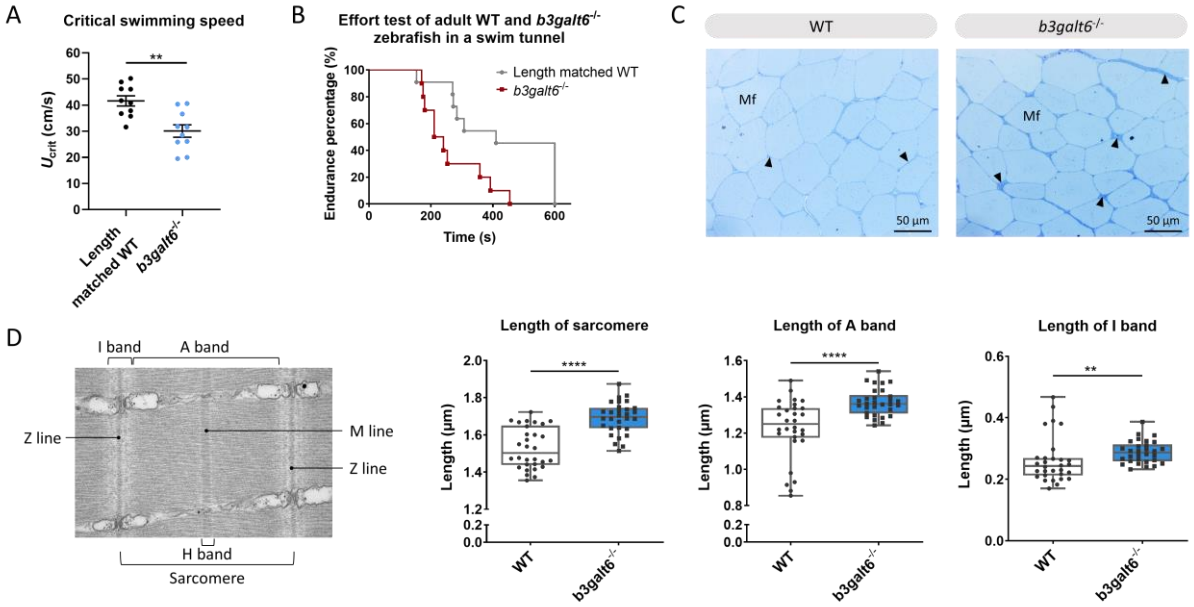

Fig. 8. Functional and structural analysis of adult WT and *b3galt6*$^{-/-}$ zebrafish muscle. (**A**) The critical swimming speed and (**B**) the endurance performance was determined for *b3galt6*$^{-/-}$ and length-matched WT zebrafish. (**C**) Semi-thin cross sections, stained with toluidine blue, demonstrate the presence of a thicker endomysium (arrowhead), located between the muscle fibers (Mf) at the horizontal myoseptum of *b3galt6*$^{-/-}$ zebrafish at the age of five months. (**D**) Transmission electron microscope structure of a sarcomere with indications of the Z and M line and A, I and H band. The sarcomere length was determined at 5 different loci per semi-thin section, for 6 semi-thin originating coming from 3 different zebrafish per genotype (N=30). A significant increase in sarcomere length for *b3galt6*$^{-/-}$ is noted. Furthermore, both the A and I band show an increase in length for the mutant zebrafish. Data are expressed as box plots with min-to-max whiskers on which each individual data point is plotted. A Mann-Whitney U test was used to determine significance. ****P<0.0001, **P<0.01.

Discussion

In this study we developed two viable *b3galt6* KO zebrafish models using CRISPR/Cas9 mutagenesis, and performed an in-depth characterization of the biochemical, ultrastructural and phenotypical consequences of β3GalT6-deficiency on different tissues, including skin, cartilage, mineralized bone and muscle. These models currently represent the only vertebrate models available for the study of the pathogenetic consequences of β3GalT6-deficiency on tissue development and homeostasis. In both models we detected a significant reduction, yet not a complete absence in *b3galt6* mRNA expression (Fig. 1E). One possible explanation is the absence of canonical nonsense-mediated decay (NMD) in the single-exon *b3galt6* gene, due to a lack of exon junction complexes (EJCs) (36). We were unable to examine the effect of the mutations on B3galt6 protein levels and localization due to the

452 unavailability of a suitable antibody. Nevertheless, since the cmg20 and cmg22 alleles are predicted to
453 introduce a PTC respectively upstream and in the catalytic domain, residual translation of some mRNA
454 into a truncated protein is not expected to lead to the production of an active enzyme. β3galt6 is a key
455 enzyme in the biosynthesis of the common linkage region of PGs, and reduced levels of active enzyme
456 are thus expected to equally affect the biosynthesis of HS and CS/DS GAG chains. We therefore
457 quantified the disaccharide concentrations in bone, muscle and skin of adult *b3galt6*$^{-/-}$ zebrafish by
458 means of a combination of enzymatic digestion and anion-exchange HPLC. This revealed a distinct, and
459 relatively proportional decrease in the concentration of CS, DS, hybrid CS/DS and HS moieties in all
460 examined tissues, compared to age-matched WT zebrafish (Table 1). Nonetheless, low amounts of
461 GAGs were still produced in the KO zebrafish in absence of upregulation of other galactosyltransferase
462 member(s) from the *b3galt* family or by other linkage-enzymes (Fig. S6). Together with the previous
463 demonstration that the other five β3GalT human enzymes (e.g. β3GalT1, β3GalT2,
464 β3GalT3/β3GalNAcT1, β3GalT4 and β3GalT5) are involved in the biosynthesis of glycoproteins and
465 glycolipids (11), compensation for galactosyltransferase II deficiency in zebrafish by other *b3galt* family
466 members is unlikely. Chinese hamster ovary *B3galt6* KO cells were also shown to be capable of
467 producing GAGs, in contrast to *Xylt2*, *B4galt7* or *B3gat3* KO cells (37). The recent identification of the
468 presence of a non-canonical trisaccharide linkage region, lacking one Gal residue (GlcA-Gal-Xyl-*O*-), as
469 a minor constituent in the PG bikunin in the urine of healthy human individuals (28), prompted us to
470 examine the composition of the GAG linkage region in our *b3galt6* KO zebrafish models, by analyzing
471 protein extracts from adult *b3galt6*$^{-/-}$ and WT zebrafish via LC-MS/MS. This led to the striking finding
472 that the few detected PGs in the *b3galt6*$^{-/-}$ zebrafish all presented with a trisaccharide PG linkage
473 region, consisting of only one Gal (Fig. 2B) (Table S6). Further *in vitro* analysis indicated that GlcAT-
474 I/B3GAT3 is capable of adding a GlcA to Gal-Xyl-*O*- (Fig. S8). This observation might explain the
475 phenotypic differences observed between GalT-II/B3GALT6 deficiency and deficiencies of the other
476 linkage region enzymes, for which such a rescue mechanism might be absent. This hypothesis is
477 supported by the lack of GAGs in the Chinese hamster ovary *Xylt2*, *B4galt7* or *B3gat3* KO cells and by
478 the lethal phenotype observed in the *b4galt7* KO zebrafish model (38). At present, we have no
479 information on the length of the GAG chains attached to the trisaccharide linkage region or the
480 composition and the possible modifications of these HS and CS/DS chains. As such, the GAG structure,
481 length and modifications in the *b3galt6*$^{-/-}$ zebrafish might be different from the ones in WT zebrafish.

482 HSPGs and CS/DSPGs are essential macromolecules for the development, signaling and homeostasis
483 of many tissues. It therefore comes as no surprise that defects in linkage region biosynthesis can affect
484 many organs. Endochondral ossification of cartilage (forming chondral bones) for example is a multi-
485 staged process that must be coordinated in space and time. CS/DSPGs and HSPGS, which have key

486 roles in modulating signaling events during vertebrate skeletal development, are expressed in a
487 spatially and temporally highly controlled manner (24), thus regulating the timing of endochondral
488 ossification. Genetic defects disrupting PG synthesis or structure have been shown to disrupt the
489 timing of skeletal development. Two zebrafish models with abnormal PG linkage region biosynthesis,
490 i.e. the *fam20b* and *xylt1*-deficient models, revealed partial decrease in CSPGs, which are
491 predominantly present in cartilage, and accelerated endochondral ossification, showing that CSPGs
492 can negatively regulate skeletogenic timing (24). On the other hand, a strong reduction in CSPGs and
493 partial decrease in HSPGs was noted in *b3gat3* mutant zebrafish, but this led to a delay in endochondral
494 ossification and short and disorganized cartilaginous structures (39). Our B3galt6-deficient zebrafish
495 models also show a delay in skeletal development at juvenile stages. At 20 dpf, a delay was noticed in
496 the development of cartilage and mineralized bony elements of the craniofacial structures, the
497 pectoral and caudal fin endoskeleton (Fig. 3B) (Tables S7 and S8), and these abnormalities had
498 progressed in adult zebrafish. The reduced body length, misshapen cranial bones and smaller teeth
499 observed in the head skeleton, and general skeletal dysplasia with kyphosis and scoliosis seen in the
500 vertebral column of *b3galt6*$^{-/-}$ adult zebrafish is reminiscent of the skeletal phenotype observed in
501 human β3GalT6-deficient individuals (Table 2).

502 In addition to skeletal dysplasia, we also observed abnormalities in bone mineralization. Adult mutant
503 zebrafish stained with AR showed the presence of extra intramembranous bone and extra bony
504 elements on the associated elements of the vertebral centra. On the other hand, quantitative µCT
505 analysis of the vertebral column and associated elements revealed a generalized reduction in bone
506 volume and thickness, and a relative increase in TMD after correction for reduced body length of the
507 mutant zebrafish (Fig. 6 and Fig. S13). Although it is not clear so far if the increased fracture risk in
508 spEDS-*B3GALT6* patients can be attributed to a lower bone volume combined with a higher TMD, such
509 hypothesis has been put forward for the brittle bone disorder Osteogenesis Imperfecta (OI) based on
510 observations in both patients and animal models (40, 41). In the Chihuahua (*col1a1a*$^{chi/+}$) OI zebrafish
511 model the intrafibrillar mineral platelets were shown to be smaller and more densely packed, leading
512 to an increased mineral to matrix ratio, and consequently a reduced elastic modulus-to-hardness ratio,
513 a measure for fracture toughness (41-43). In addition, in both OI patients and the mouse model *oim,*
514 reduced collagen matrix organization was shown to lead to the formation of extrafibrillar crystals,
515 which are larger compared to intrafibrillar crystals (43). Eventually, additional minerals stabilize the
516 tissue, but they do so at the cost of increased brittleness of the bone (44). In accordance, in *b3galt6*$^{-/-}$
517 zebrafish we observed an irregular collagen organization interspersed with large interfibrillar spaces
518 and electron dense spots on ultra-thin sections of skin and bone via TEM. The 'dark spots' observed in

519 the vertebral bone could be remnants of extrafibrillar mineral aggregates, contributing to increased
520 mineralization but also increased brittleness of the skeleton.

521 Abnormalities in collagen fibril organization were observed in many mutant zebrafish tissues. Besides
522 vertebral bone, irregular collagen organization was also observed in the intervertebral space,
523 intervertebral ligament, and the dermis. (Fig. 7). This strongly resembles the previously reported
524 abnormal dermal collagen fibril architecture in the skin from a β3GalT6-deficient individual (5). This
525 could be attributed to abnormalities in GAG chains of small leucine-rich PGs (SLRPs), such as the DSPGs
526 decorin and biglycan, which are known to be of particular importance for regulating collagen fibril
527 organization in connective tissues through their core protein and GAG chains (45). SLRPs are also
528 thought to influence collagen cross-linking patterns, but the mechanism by which they do so remain
529 largely unknown (45). Although similar hydroxylation levels were observed at K87 and the C-
530 telopeptide of the type I collagen α1 chain in *b3galt6*$^{-/-}$ and WT adult zebrafish (Table S9), we cannot
531 rule out that type I collagen cross-linking might still be affected.

532 In view of the observation that human β3GalT6-deficient individuals often present quite severe muscle
533 hypotonia with delayed gross motor development and reduced endurance, we also studied the effect
534 of B3galt6-deficiency on GAG synthesis in muscle, and on muscle function and ultrastructure (Fig. 8).
535 Similar to the other examined tissues, HS and CS/DS GAG concentrations were severely reduced in
536 muscle tissue. It is known that the ECM in skeletal muscle plays an important role in muscle fiber force
537 transmission, maintenance and repair. Numerous PGs, including the HSPGs syndecans 1-4, glypican-1,
538 perlecan and agrin, and CS/DSPGs, such as decorin and biglycan, are present in muscle ECM. Besides
539 their structural role, many of them are known to bind growth factors (e.g. TGFβ). Those growth factors
540 can be stored and released by the negatively charged GAGs. Certain enzymes in the ECM can cleave
541 GAG chains, thereby releasing associated growth factors, allowing their interaction in cell signaling and
542 mechanotransduction (46). The significant decrease in critical swimming speed (U_{crit}) and endurance
543 observed in the *b3galt6*$^{-/-}$ zebrafish suggest decreased muscle function (Fig. 8A-B). Further evidence
544 for an intrinsic muscle dysfunction in the *b3galt6*$^{-/-}$ model comes from semi-thin muscle sections,
545 showing an enlargement of the connective tissue sheet surrounding the muscle fibers (Fig. 8C).
546 Nevertheless, we cannot exclude that the observed skeletal malformations and/or other
547 abnormalities, such as respiratory or neuronal dysfunction, could also influence the outcome of these
548 tests.

549 **Table 2. Clinical features and ultrastructural and biochemical abnormalities observed in spEDS-**
550 ***B3GALT6* and SEMD-JL1 individuals compared to the *b3galt6*$^{-/-}$ zebrafish model.** n.a.: not available.

551 GAG: glycosaminoglycan. The columns 'spEDS-*B3GALT6*' and 'SEMD-JL1' summarize the most
552 important clinical features of all hitherto reported patients for whom this data was available (20, 47).

	Human		**Zebrafish**
	spEDS-*B3GALT6*	SEMD-JL1	*b3galt6*$^{-/-}$ mutant
General morphology			
Short stature	22/30	11/14	Reduced body length
Craniofacial dysmorphisms (e.g. midfacial hypoplasia, micrognatia)	25/30	12/14	Deformed, small and round head with shorter parietal/occipital region and underdeveloped olfactory region
Dental abnormalities	14/30	n.a.	Smaller teeth
Musculoskeletal involvement			
Bowing of limbs, metaphyseal widening or vertebral body changes	20/30	14/14	Deformities of the fin skeleton
Bone fragility with spontaneous fractures	19/30	0/3	Extra intramembranous bone, lower degree of collagen type I fibril organization and higher TMD after correction for smaller size
Joint contractures (especially hands)	23/30	5/14	Pectoral fins point upwards
Joint hypermobility	26/30	6/14	n.a.
Kyphoscoliosis	23/30	13/14	Kyphosis and scoliosis
Muscle hypotonia	18/30	1/14	Reduced critical swimming speed and endurance
Skin features			
Skin hyperextensibility	19/30	2/14	n.a.
Biochemical findings			
Reduced GAG synthesis	9/9	4/4 (3/4; < HS but > CS/DS)	Reduced GAG production
Ultrastructural findings			
Loosely packed collagen fibrils	1/1	n.a.	Disturbed collagen fibril organization in bone and loosely packed collagen fibrils in the dermis

553 Taken together, we generated and characterized the first *b3galt6* KO zebrafish models and show that
554 their phenotype largely mimics that of human β3Galt6-deficiency. A strong reduction in HS, CS and DS
555 GAG concentration was observed in *b3galt6*$^{-/-}$ zebrafish. Yet, we did observe a small amount of GAGs
556 being produced with a unique trisaccharide PG linkage region. Furthermore, we showed that a lack of
557 B3galt6 causes disturbances in collagen fibril organization in skin, ligament and bone, with the latter

558 also showing abnormalities in mineralization, and leads to structural and functional abnormalities of
559 the muscle. These KO zebrafish can serve as useful models to further unravel the underlying
560 pathogenic mechanisms of this complex multisystemic disorder and serve as a tool for the
561 development and evaluation of possible therapeutic interventions, such as the stimulation of intrinsic
562 compensational mechanisms for the production of PGs.

563

564

565 ## Material and Methods

566 Zebrafish Maintenance

567 Wild-type (AB strain) and *b3galt6* knock-out zebrafish lines were reared and maintained by standard
568 protocols (48). All animal studies were performed in agreement with EU Directive 2010/63/EU for
569 animals, permit number: ECD 16/18. All zebrafish used in a single experiment were bred at the same
570 density. All efforts were made to minimize pain, distress and discomfort.

571 Alcian blue and alizarin red staining

572 Twenty-day-old larvae (n=10) and five-month-old WT and *b3galt6*$^{-/-}$ (n=5) adult zebrafish were
573 stained as previously described (38). See Supplementary Information for details.

574 µCT scanning analysis

575 Whole-body µCT scans of four-month-old WT (n=5) and *b3galt6*$^{-/-}$ (n=5) siblings were acquired on a
576 SkyScan 1275 (Bruker, Kontich, Belgium) using the following scan parameters: 0.25 mm aluminum
577 filter, 50 kV, 160 µA, 65 ms integration time, 0.5° rotation step, 721 projections/360°, 5 m 57 s scan
578 duration and 21 µm voxel size. DICOM files of individual zebrafish were segmented in MATLAB using
579 custom FishCuT software and data were analyzed and corrected for standard length in the R statistical
580 environment, as previously described (33).

581 Histology and transmission electron microscopy

582 Zebrafish bone, consisting of the last transitional vertebra and two consecutive caudal vertebrae (49,
583 50), skin, at the lateral line below the dorsal fin, and muscle samples, located dorsolateral underneath
584 the dorsal fin, dissected from five-month-old WT (n=5) and *b3galt6*$^{-/-}$ (n=5) zebrafish, were fixed and
585 embedded in epon following the procedures outlined by Huysseune and Sire (51).

586 Swim tunnel experiments

587 Ten WT (five months) and ten *b3galt6*$^{-/-}$ zebrafish (eight months), were selected based on their similar
588 (not significantly different) length and weight. The critical swimming speed (U_{crit}) was measured in a
589 swim tunnel for both WT and *b3galt6*$^{-/-}$ zebrafish as previously described (52). Furthermore, the
590 endurance of each zebrafish was tested by means of an effort test in the swim tunnel. Each zebrafish
591 had a three minute warm-up and after the third minute, the speed increased until 37 cm/s for
592 maximum 7 minutes. When the zebrafish was not able to swim anymore, the test was stopped.

593 Collagen crosslinking analysis

594 The collagen crosslinking was analyzed in the dissected vertebral column (excluding Weberian
595 apparatus and urostyle) from five-month-old wild-type (n=5) and *b3galt6*$^{-/-}$ (n=5) siblings as described
596 before in Gistelinck *et al.* (40).

597 Disaccharide composition analysis of CS, DS, and HS chains

598 The level of total disaccharides from CS, DS, and HS in bone, muscle and skin tissues from nine-month-
599 old zebrafish (n=5) were determined as described previously (53, 54).

600 Glycopeptide preparation and analysis

601 **LC-MS/MS sample preparation -** CS- and HS-glycopeptides were purified from six-month-old WT (n=3)
602 and *b3galt6*$^{-/-}$ (n=3) zebrafish using a combination of extraction, trypsin digestion and anion exchange
603 chromatography, slightly modified (see Supplementary Information) from previously described
604 protocols (27, 55).

605 **LC-MS/MS analysis -** The samples were analyzed on an Orbitrap Fusion mass spectrometer coupled to
606 an Easy-nLC 1200 liquid chromatography system (Thermo Fisher Scientific., Waltham, MA) (see
607 Supplementary Information). Nanospray Flex ion source was operated in positive ionization mode and
608 three separate higher-energy collision-induced dissociation (HCD) MS/MS spectra were recorded for
609 each precursor ion (27, 55).

610 **LC-MS/MS data analysis -** The glycopeptide files were analyzed using both manual interpretation and
611 automated Mascot searches for GAG-glycopeptides. The files were manually interpreted using the
612 Xcalibur software (Thermo Fisher Scientific). Database searches were performed against *Danio rerio* in
613 the UniProtKB/Swiss-Prot database and NCBI using Mascot Distiller (version 2.6.1.0, Matrix Science,
614 London, U.K) and an in-house Mascot server (version 2.5.1). Glycan structures with very small mass
615 differences were manually evaluated at the MS2-level.

616 GlcAT-I assay

617 GlcA-transferase assay was carried out by the methodology as previously described (12, 56, 57), with
618 slight modifications.

619 Detailed information regarding the procedures used is provided in SI Appendix, Supplementary
620 Material and Methods.

621

622 Competing interests

623 The authors declare no competing interests.

624

625 Acknowledgements

626 We would like to thank the TEM facility of the Nematology Research Unit, member of the UGent TEM-
627 Expertise center (life sciences). We are grateful to Hanna De Saffel and Petra Vermassen for their
628 technical assistance on processing the TEM samples. The LC-MS/MS analyses were performed at the
629 BioMS node at the Proteomics Core Facility, Sahlgrenska Academy, University of Gothenburg with
630 support from the Swedish National Infrastructure for Biological Mass Spectrometry (BioMS), funded
631 by the Swedish Research Council.

632

633 Funding

634 DS and FM are a postdoctoral fellow and a senior clinical investigator, respectively, of the Research
635 Foundation Flanders (FWO), Belgium. This work was supported by a Methusalem Grant
636 (BOFMET2015000401) from the Ghent University to Prof. Anne De Paepe, by grants from the FWO to
637 DS (12Q5917N) and to FM (1842318N) and by grant (2017-00955) from the Swedish Research Council
638 to FN and GL. CG is supported at the UW by a post-doctoral fellowship of the Belgian American
639 Educational Fund (BAEF). This work was further supported by a Grant-in-Aid for Scientific Research (C)
640 19K07054 (to SM) from the Japan Society for the Promotion of Science, Japan; by the Takeda Science
641 Foundation (to SM); Grant-in Aid for Research Center for Pathogenesis of Intractable Diseases from
642 the Research Institute of Meijo University (SM and SY).

643

644

645

646 ## References

647 1. Prydz K, Dalen KT. Synthesis and sorting of proteoglycans - Commentary. J Cell Sci.
648 2000;113(2):193-205.
649 2. Couchman JR, Pataki CA. An introduction to proteoglycans and their localization. J Histochem
650 Cytochem. 2012;60(12):885-97.
651 3. Lindahl U, Couchman J, Kimata K, Esko JD. Proteoglycans and Sulfated Glycosaminoglycans.
652 In: rd, Varki A, Cummings RD, Esko JD, Stanley P, Hart GW, et al., editors. Essentials of Glycobiology.
653 Cold Spring Harbor (NY)2015. p. 207-21.
654 4. Selleck SB. Proteoglycans and pattern formation: sugar biochemistry meets developmental
655 genetics. Trends Genet. 2000;16(5):206-12.
656 5. Malfait F, Kariminejad A, Van Damme T, Gauche C, Syx D, Merhi-Soussi F, et al. Defective
657 Initiation of Glycosaminoglycan Synthesis due to B3GALT6 Mutations Causes a Pleiotropic Ehlers-
658 Danlos-Syndrome-like Connective Tissue Disorder. Am J Hum Genet. 2013;92(6):935-45.
659 6. Sugahara K, Mikami T, Uyama T, Mizuguchi S, Nomura K, Kitagawa H. Recent advances in the
660 structural biology of chondroitin sulfate and dermatan sulfate. Curr Opin Struct Biol. 2003;13(5):612-
661 20.
662 7. Kusche-Gullberg M, Kjellen L. Sulfotransferases in glycosaminoglycan biosynthesis. Curr Opin
663 Struct Biol. 2003;13(5):605-11.
664 8. Bui C, Ouzzine M, Talhaoui I, Sharp S, Prydz K, Coughtrie MW, et al. Epigenetics: methylation-
665 associated repression of heparan sulfate 3-O-sulfotransferase gene expression contributes to the
666 invasive phenotype of H-EMC-SS chondrosarcoma cells. FASEB J. 2010;24(2):436-50.
667 9. Gotting C, Kuhn J, Zahn R, Brinkmann T, Kleesiek K. Molecular cloning and expression of
668 human UDP-d-Xylose:proteoglycan core protein beta-d-xylosyltransferase and its first isoform XT-II. J
669 Mol Biol. 2000;304(4):517-28.
670 10. Almeida R, Levery SB, Mandel U, Kresse H, Schwientek T, Bennett EP, et al. Cloning and
671 expression of a proteoglycan UDP-galactose:beta-xylose beta1,4-galactosyltransferase I. A seventh
672 member of the human beta4-galactosyltransferase gene family. J Biol Chem. 1999;274(37):26165-71.
673 11. Bai X, Zhou D, Brown JR, Crawford BE, Hennet T, Esko JD. Biosynthesis of the linkage region of
674 glycosaminoglycans: cloning and activity of galactosyltransferase II, the sixth member of the beta 1,3-
675 galactosyltransferase family (beta 3GalT6). J Biol Chem. 2001;276(51):48189-95.
676 12. Kitagawa H, Tone Y, Tamura J, Neumann KW, Ogawa T, Oka S, et al. Molecular cloning and
677 expression of glucuronyltransferase I involved in the biosynthesis of the glycosaminoglycan-protein
678 linkage region of proteoglycans. J Biol Chem. 1998;273(12):6615-8.

679 13. Wen J, Xiao J, Rahdar M, Choudhury BP, Cui J, Taylor GS, et al. Xylose phosphorylation
680 functions as a molecular switch to regulate proteoglycan biosynthesis. Proc Natl Acad Sci U S A.
681 2014;111(44):15723-8.
682 14. Jones KL, Schwarze U, Adam MP, Byers PH, Mefford HC. A homozygous B3GAT3 mutation
683 causes a severe syndrome with multiple fractures, expanding the phenotype of linkeropathy
684 syndromes. Am J Med Genet A. 2015;167A(11):2691-6.
685 15. Guo MH, Stoler J, Lui J, Nilsson O, Bianchi DW, Hirschhorn JN, et al. Redefining the progeroid
686 form of Ehlers-Danlos syndrome: report of the fourth patient with B4GALT7 deficiency and review of
687 the literature. Am J Med Genet A. 2013;161A(10):2519-27.
688 16. Nakajima M, Mizumoto S, Miyake N, Kogawa R, Iida A, Ito H, et al. Mutations in B3GALT6,
689 which encodes a glycosaminoglycan linker region enzyme, cause a spectrum of skeletal and
690 connective tissue disorders. Am J Hum Genet. 2013;92(6):927-34.
691 17. Malfait F, Kariminejad A, Van Damme T, Gauche C, Syx D, Merhi-Soussi F, et al. Defective
692 initiation of glycosaminoglycan synthesis due to B3GALT6 mutations causes a pleiotropic Ehlers-
693 Danlos-syndrome-like connective tissue disorder. Am J Hum Genet. 2013;92(6):935-45.
694 18. Malfait F, Francomano C, Byers P, Belmont J, Berglund B, Black J, et al. The 2017 international
695 classification of the Ehlers-Danlos syndromes. Am J Med Genet C Semin Med Genet. 2017;175(1):8-
696 26.
697 19. Ritelli M, Chiarelli N, Zoppi N, Dordoni C, Quinzani S, Traversa M, et al. Insights in the
698 etiopathology of galactosyltransferase II (GalT-II) deficiency from transcriptome-wide expression
699 profiling of skin fibroblasts of two sisters with compound heterozygosity for two novel B3GALT6
700 mutations. Mol Genet Metab Rep. 2015;2:1-15.
701 20. Van Damme T, Pang X, Guillemyn B, Gulberti S, Syx D, De Rycke R, et al. Biallelic B3GALT6
702 mutations cause spondylodysplastic Ehlers-Danlos syndrome. Hum Mol Genet. 2018;27(20):3475-87.
703 21. Santoriello C, Zon LI. Hooked! Modeling human disease in zebrafish. J Clin Invest.
704 2012;122(7):2337-43.
705 22. Dooley K, Zon LI. Zebrafish: a model system for the study of human disease. Curr Opin Genet
706 Dev. 2000;10(3):252-6.
707 23. Eames BF, Singer A, Smith GA, Wood ZA, Yan YL, He X, et al. UDP xylose synthase 1 is
708 required for morphogenesis and histogenesis of the craniofacial skeleton. Dev Biol. 2010;341(2):400-
709 15.
710 24. Eames BF, Yan YL, Swartz ME, Levic DS, Knapik EW, Postlethwait JH, et al. Mutations in
711 fam20b and xylt1 reveal that cartilage matrix controls timing of endochondral ossification by
712 inhibiting chondrocyte maturation. PLoS Genet. 2011;7(8):e1002246.

713 25. Amsterdam A, Nissen RM, Sun Z, Swindell EC, Farrington S, Hopkins N. Identification of 315
714 genes essential for early zebrafish development. Proc Natl Acad Sci U S A. 2004;101(35):12792-7.
715 26. Nissen RM, Amsterdam A, Hopkins N. A zebrafish screen for craniofacial mutants identifies
716 wdr68 as a highly conserved gene required for endothelin-1 expression. BMC Dev Biol. 2006;6:28.
717 27. Noborn F, Gomez Toledo A, Sihlbom C, Lengqvist J, Fries E, Kjellen L, et al. Identification of
718 chondroitin sulfate linkage region glycopeptides reveals prohormones as a novel class of
719 proteoglycans. Mol Cell Proteomics. 2015;14(1):41-9.
720 28. Persson A, Nilsson J, Vorontsov E, Noborn F, Larson G. Identification of a non-canonical
721 chondroitin sulfate linkage region trisaccharide. Glycobiology. 2019;29(5):366-71.
722 29. Nash RDM, Valencia AH, Geffen AJ. The origin of Fulton's condition factor - Setting the record
723 straight. Fisheries. 2006;31(5):236-8.
724 30. Arratia G, Schultze HP. Reevaluation of the caudal skeleton of certain actinopterygian fishes:
725 III. Salmonidae. Homologization of caudal skeletal structures. J Morphol. 1992;214(2):187-249.
726 31. McMenamin SK, Chandless MN, Parichy DM. Working with zebrafish at postembryonic
727 stages. Methods Cell Biol. 2016;134:587-607.
728 32. Parichy DM, Elizondo MR, Mills MG, Gordon TN, Engeszer RE. Normal table of postembryonic
729 zebrafish development: staging by externally visible anatomy of the living fish. Dev Dyn.
730 2009;238(12):2975-3015.
731 33. Hur M, Gistelinck CA, Huber P, Lee J, Thompson MH, Monstad-Rios AT, et al. MicroCT-based
732 phenomics in the zebrafish skeleton reveals virtues of deep phenotyping in a distributed organ
733 system. Elife. 2017;6.
734 34. Gistelinck C, Gioia R, Gagliardi A, Tonelli F, Marchese L, Bianchi L, et al. Zebrafish Collagen
735 Type I: Molecular and Biochemical Characterization of the Major Structural Protein in Bone and Skin.
736 Sci Rep. 2016;6:21540.
737 35. Plaut I. Effects of fin size on swimming performance, swimming behaviour and routine
738 activity of zebrafish Danio rerio. J Exp Biol. 2000;203(Pt 4):813-20.
739 36. Wittkopp N, Huntzinger E, Weiler C, Sauliere J, Schmidt S, Sonawane M, et al. Nonsense-
740 mediated mRNA decay effectors are essential for zebrafish embryonic development and survival. Mol
741 Cell Biol. 2009;29(13):3517-28.
742 37. Chen YH, Narimatsu Y, Clausen TM, Gomes C, Karlsson R, Steentoft C, et al. The GAGOme: a
743 cell-based library of displayed glycosaminoglycans. Nat Methods. 2018;15(11):881-8.
744 38. Delbaere S, Van Damme T, Syx D, Symoens S, Coucke P, Willaert A, et al. Hypomorphic
745 zebrafish models mimic the musculoskeletal phenotype of β4GalT7-deficient Ehlers-Danlos
746 syndrome. Matrix Biol. 2019.

747 39. Holmborn K, Habicher J, Kasza Z, Eriksson AS, Filipek-Gorniok B, Gopal S, et al. On the roles
748 and regulation of chondroitin sulfate and heparan sulfate in zebrafish pharyngeal cartilage
749 morphogenesis. J Biol Chem. 2012;287(40):33905-16.
750 40. Gistelinck C, Witten PE, Huysseune A, Symoens S, Malfait F, Larionova D, et al. Loss of Type I
751 Collagen Telopeptide Lysyl Hydroxylation Causes Musculoskeletal Abnormalities in a Zebrafish Model
752 of Bruck Syndrome. J Bone Miner Res. 2016;31(11):1930-42.
753 41. Fiedler IAK, Schmidt FN, Wolfel EM, Plumeyer C, Milovanovic P, Gioia R, et al. Severely
754 Impaired Bone Material Quality in Chihuahua Zebrafish Resembles Classical Dominant Human
755 Osteogenesis Imperfecta. Journal of Bone and Mineral Research. 2018;33(8):1489-99.
756 42. Bishop N. Bone Material Properties in Osteogenesis Imperfecta. J Bone Miner Res.
757 2016;31(4):699-708.
758 43. Viguet-Carrin S, Garnero P, Delmas PD. The role of collagen in bone strength. Osteoporos Int.
759 2006;17(3):319-36.
760 44. Grabner B, Landis WJ, Roschger P, Rinnerthaler S, Peterlik H, Klaushofer K, et al. Age- and
761 genotype-dependence of bone material properties in the osteogenesis imperfecta murine model
762 (oim). Bone. 2001;29(5):453-7.
763 45. Kalamajski S, Oldberg A. The role of small leucine-rich proteoglycans in collagen
764 fibrillogenesis. Matrix Biol. 2010;29(4):248-53.
765 46. Gillies AR, Lieber RL. Structure and function of the skeletal muscle extracellular matrix.
766 Muscle Nerve. 2011;44(3):318-31.
767 47. Caraffi SG, Maini I, Ivanovski I, Pollazzon M, Giangiobbe S, Valli M, et al. Severe Peripheral
768 Joint Laxity is a Distinctive Clinical Feature of Spondylodysplastic-Ehlers-Danlos Syndrome (EDS)-
769 B4GALT7 and Spondylodysplastic-EDS-B3GALT6. Genes (Basel). 2019;10(10).
770 48. Gistelinck C, Kwon RY, Malfait F, Symoens S, Harris MP, Henke K, et al. Zebrafish type I
771 collagen mutants faithfully recapitulate human type I collagenopathies. Proc Natl Acad Sci U S A.
772 2018;115(34):E8037-E46.
773 49. Bird NC, Mabee PM. Developmental morphology of the axial skeleton of the zebrafish, Danio
774 rerio (Ostariophysi: Cyprinidae). Dev Dyn. 2003;228(3):337-57.
775 50. Morin-Kensicki EM, Melancon E, Eisen JS. Segmental relationship between somites and
776 vertebral column in zebrafish. Development. 2002;129(16):3851-60.
777 51. Huysseune A, Sire JY. Bone and cartilage resorption in relation to tooth development in the
778 anterior part of the mandible in cichlid fish: a light and TEM study. Anat Rec. 1992;234(1):1-14.
779 52. Brett JR. The Respiratory Metabolism and Swimming Performance of Young Sockeye Salmon.
780 J Fish Res Board Can. 1964;21(5):1183-226.

781 53. Mizumoto S, Mikami T, Yasunaga D, Kobayashi N, Yamauchi H, Miyake A, et al. Chondroitin 4-
782 O-sulfotransferase-1 is required for somitic muscle development and motor axon guidance in
783 zebrafish. Biochem J. 2009;419(2):387-99.
784 54. Mizumoto S, Sugahara K. Glycosaminoglycan chain analysis and characterization
785 (glycosylation/epimerization). Methods Mol Biol. 2012;836:99-115.
786 55. Noborn F, Gomez Toledo A, Green A, Nasir W, Sihlbom C, Nilsson J, et al. Site-specific
787 identification of heparan and chondroitin sulfate glycosaminoglycans in hybrid proteoglycans. Sci
788 Rep. 2016;6:34537.
789 56. Baasanjav S, Al-Gazali L, Hashiguchi T, Mizumoto S, Fischer B, Horn D, et al. Faulty initiation of
790 proteoglycan synthesis causes cardiac and joint defects. Am J Hum Genet. 2011;89(1):15-27.
791 57. Job F, Mizumoto S, Smith L, Couser N, Brazil A, Saal H, et al. Functional validation of novel
792 compound heterozygous variants in B3GAT3 resulting in severe osteopenia and fractures: expanding
793 the disease phenotype. BMC Med Genet. 2016;17(1):86.

794